

Real-time simulation enabled navigation control of magnetic soft continuum robots in confined lumens

Dezhong Tong^{1,2,†}, Zhuonan Hao^{3,†}, Jiyu Li^{1,†}, Boxi Sun¹, Mingchao Liu^{4,*},
Liu Wang^{1,*}, Weicheng Huang^{5,*}

¹*CAS Key Laboratory of Mechanical Behavior and Design of Materials, Department of Modern Mechanics, University of Science and Technology of China, Hefei 230026, PR China*

²*Department of Material Science and Engineering, University of Michigan, Ann Arbor, Ann Arbor, Michigan, 48105, USA*

³*Department of Mechanical and Aerospace Engineering, University of California, Los Angeles, Los Angeles, California 90095, United States*

⁴*Department of Mechanical Engineering, University of Birmingham, Birmingham B15 2TT, UK*

⁵*School of Engineering, Newcastle University, Newcastle upon Tyne, NE1 7RU, UK*

[†]*These authors contributed equally to this work.*

** Corresponding authors:*

m.liu.2@bham.ac.uk (M.L.)

wangliu05@outlook.com (L.W.)

weicheng.huang@ncl.ac.uk (W.H.).

Abstract

Magnetic soft continuum robots (MSCRs) have emerged as a promising technology for minimally invasive interventions, offering enhanced dexterity and remote-controlled navigation in confined lumens. Unlike conventional guidewires with pre-shaped tips, MSCRs feature a magnetic tip that actively bends under applied magnetic fields. Despite extensive studies in modeling and simulation, achieving real-time navigation control of MSCRs in confined lumens remains a significant challenge. The primary reasons are due to robot-lumen contact interactions and computational limitations in modeling MSCR nonlinear behavior under magnetic actuation. Existing approaches, such as Finite Element Method (FEM) simulations and energy-minimization techniques, suffer from high computational costs and oversimplified contact interactions, making them impractical for real-world applications. In this work, we develop a real-time simulation and navigation control framework that integrates hard-magnetic elastic rod theory, formulated within the Discrete Differential Geometry (DDG) framework, with an order-reduced contact handling strategy. Our approach captures large deformations and complex interactions while maintaining computational efficiency. Next, the navigation control problem is formulated as an inverse design task, where optimal magnetic fields are computed in real time by minimizing the constrained forces and enhancing navigation accuracy. We validate the proposed framework through comprehensive numerical simulations and experimental studies, demonstrating its robustness, efficiency, and accuracy. The results show that our method significantly reduces computational costs while maintaining high-fidelity modeling, making it feasible for real-time deployment in clinical settings. Our work addresses key limitations in MSCR navigation control, paving the way for safer and more reliable clinical translation of MSCR technology for interventional surgeries.

Keywords: Magnetic soft continuum robot, Hard magnetic elastica, Discrete simulation, Model-based control, Confined lumen

1. Introduction

Interventional surgeries are a standard treatment for vascular and gastrointestinal diseases, offering reduced recovery times and fewer complications compared to traditional open surgeries (Muller et al., 1992). In endovascular interventions such as thrombectomy and aneurysm embolization, a mechanical guidewire

with a pre-shaped tip is inserted through a small incision into the femoral artery and manually navigated under fluoroscopic guidance to reach the target site (Munich et al., 2019). However, the pre-shaped tip of mechanical guidewires poses significant challenges in navigating tortuous or branching confined lumens (Goyal et al., 2016; Appireddy et al., 2016). The reliance on trial-and-error maneuvering increases procedure time, risks vessel wall injury, and exposes both the patient and surgeon to prolonged fluoroscopic radiation (Zhao et al., 2022; Duan et al., 2023).

To overcome these challenges, magnetic soft continuum robots (MSCRs) have recently emerged as a promising alternative. Distinct from the pre-shaped tip, MSCRs feature a magnetically bendable tip that enhances its remotely-controlled navigation in confined lumens (as shown in Fig. 1(A)) (Wu et al., 2020; Kim and Zhao, 2022; Yang et al., 2023a). Constructed from soft polymers embedded with hard-magnetic particles such as neodymium iron boron (NdFeB), the MSCR's tip actively bends in response to actuation magnetic fields (Fig. 1(B)) (Kim et al., 2019). This capability enhances maneuverability in complex and confined anatomical pathways, including cerebral vessels (Kim et al., 2022), the aorta (Wang et al., 2022), and the colon (Martin et al., 2020), surpassing traditional guidewires. By eliminating the need for repeated manual adjustments, MSCRs significantly reduce both procedure time and radiation exposure for patients and surgeons (Hwang et al., 2020; Gunduz et al., 2021).

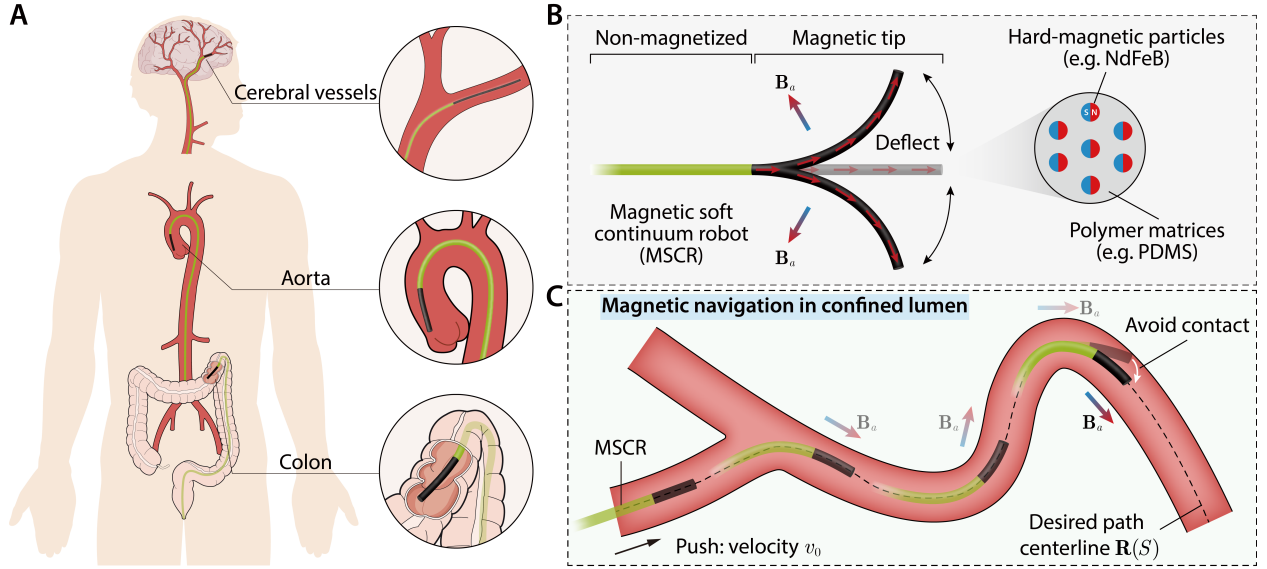


Figure 1: Schematic of a magnetic soft continuum robot (MSCR) navigating through the confined lumen within the biological systems. (A) Anatomical illustration of luminal structures, including cerebral vessels, the aorta, and the colon. The MSCR demonstrates adaptability for operation within diverse pathways. (B) Composition of the MSCR. The magnetic tip (black), fabricated by embedding hard-magnetic particles (e.g. NdFeB) within polymer matrices (e.g. PDMS), deflects in response to an actuation magnetic field B_a . (C) The MSCR is pushed at the proximal end with velocity v_0 . By controlling the actuation magnetic fields B_a , the MSCR is steered along the desired path (centerline $R(S)$) through the confined lumen without the tip contact with the lumen wall.

The promising potential of MSCRs has driven extensive research into their magneto-mechanical behavior through theoretical modeling and numerical simulation. Early studies by Zhao et al. (2019) introduced a hyperelastic constitutive model to describe the interactions between dispersed magnetic particles and applied magnetic fields using magnetic Cauchy stresses. Wang et al. (2020) extended this by developing a hard-magnetic elastica model to describe the large deflections under uniform magnetic fields, providing analytical solutions for MSCR deformations. Further refinements have included extensible rod models that accounts for stretching deformations (Chen et al., 2020a,b; Chen and Wang, 2020) and a beam-based framework incorporating three-dimensional (3D) Finite Element Method (FEM) simulation (Yan et al., 2022). In addition, more complex approaches have incorporated nonlinear large deformation analyses, using Kirchhoff-

like rod models (Sano et al., 2022), Euler-angle-based formulations (Chen et al., 2021), and models that consider deformable cross-sections (Li et al., 2023).

Beyond analytical modeling, numerical methods such as finite difference approximations (Wang et al., 2021), magnetic lattice models (Ye et al., 2021), mesh-free models (Liu et al., 2023), reduced-order FEM model (Moezi et al., 2024) have been widely employed to solve complex MSCR deformation problems. In addition, a total Lagrangian (TL) finite element formulation is constructed based on micropolar theory to capture the asymmetric stress response and size-dependent behavior of soft hard-magnetic beams (Dadgar-Rad et al., 2024). At the microstructural level, Garcia-Gonzalez and Hossain (2021) incorporated dipole-dipole interactions of embedded magnetic particles, while Stewart and Anand (2023) developed finite deformation models for hard-magnetic viscoelastic materials. Collectively, these studies have established a solid theoretical foundation for understanding the magneto-mechanical behavior of MSCRs in static and uniform magnetic fields.

Recent advances have expanded MSCR modeling to include dynamic behavior and nonuniform magnetic fields. For instance, Huang et al. (2023a,b) formulated a discrete magneto-elastic rod model based on Discrete Elastic Rods (DER) algorithm to analyze the dynamics of MSCR under magnetic actuation. High-order dynamic modeling using absolute nodal coordinate formulation has also been explored by Wang et al. (2024). Li and Wang (2024) used energy minimization method to describe large deformations in nonuniform magnetic environments. Yao et al. (2023) integrated deep reinforcement learning into Cosserat rod-based simulations to develop dynamic control strategies.

Despite these advances, precise navigation control of MSCRs under magnetic actuation still faces significant challenges (Yang et al., 2023b). A key challenge arises from the complex contact interactions between the MSCR’s tip and the surrounding lumen, such as blood vessel walls (Khoshnam et al., 2015; Wang et al., 2022). These interactions are particularly critical in confined lumens where unintended contact can alter MSCR’s trajectory and compromise navigation accuracy. More critically, excessive contact forces increase the risk of lumen injury or rupture, leading to severe complications (Wang et al., 2015). However, existing models oversimplify or neglect these contact interactions, limiting their ability to provide navigation control in real-world scenarios (Li et al., 2024b).

Another challenge lies in the computational demands of modeling the MSCR’s dynamic behavior in confined lumens. While FEM and lattice-based models have been widely used to analyze large deformations of MSCR, their high computational cost make them impractical for real-time applications (Zhao et al., 2019; Ye et al., 2021; Dadgar-Rad and Hossain, 2022). Similarly, energy minimization approaches struggle with efficiently updating contact conditions and adjusting magnetic fields in real-time, limiting their applicability in dynamic and confined environments (Li et al., 2024a). These computational limitations pose a significant barrier to real-time navigation control, where the ability to rapidly predict MSCR deformations and adjust magnetic fields is critical for safe and effective operation in confined lumens. (Fig. 1(C)).

In this work, we address these challenges by developing a real-time simulation and navigation control framework for MSCRs in confined lumens. Our approach integrates hard-magnetic elastic rod theory with penalty energy-based contact handling, enabling computationally efficient and accurate modeling of MSCR deformations under real-time magnetic actuation. As shown in Fig. 1(C), the MSCR will be pushed into the lumen without any external twisting applied on the pushing end. By dynamically adjusting an external magnetic field, the deflection of the MSCR tip can be controlled during navigation. To ensure safe and effective navigation, we formulate a mechanics model-based control framework that compute the optimal magnetic field in real-time based on MSCR’s geometric and material properties, as well as the surrounding lumen constraints. Consequently, the MSCR can autonomously adjust its trajectory to maintain alignment with the lumen’s centerline, minimizing contact forces and reducing the risk of vessel wall injury. We validate the performance of our model-based control framework through numerical simulations and experimental studies across various lumen geometries. The results demonstrate that our method achieves robust, efficient, and high-fidelity real-time performance, significantly improving MSCR navigation capability in complex environments.

This article is organized as follows. Section 2 presents the analytical derivation of the governing equations for a hard-magnetic rod navigating within a confined lumen. In Section 3, we develop a numerical framework

that integrates nonlinear elasticity, magnetic actuation, and non-penetration contact handling to solve these equations. Section 4 details how the model-based control problem is reformulated as an inverse design problem in mechanics. Section 5 provides a comprehensive numerical study of the proposed control method, supplemented by experimental validation. Finally, we conclude in Section 6, discussing potential applications of the developed framework for MSCR control in medical interventions.

2. Theoretical model

In this section, we derive the governing equations for the geometrically nonlinear deformations of a MSCR navigating through a confined lumen. The MSCR is modeled as a 3D hard-magnetic elastic rod, while the confined lumen is represented as a curved tube. We begin by formulating the mechanical model based on the classical Kirchhoff equations for an one-dimensional (1D) slender structure (Audoly and Pomeau, 2000), then incorporate external magnetic forces and contact interactions with the lumen walls.

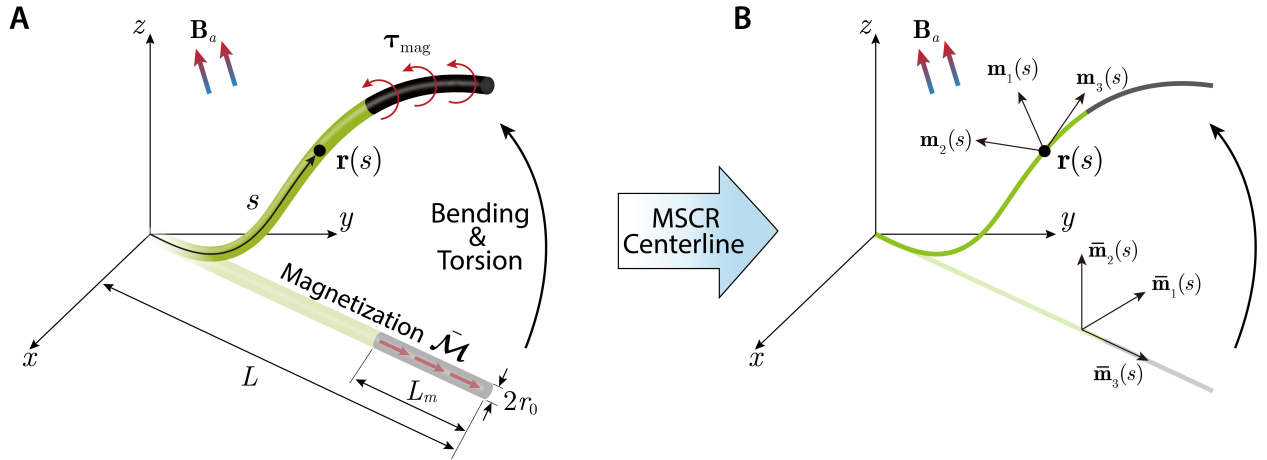


Figure 2: Simplified representation of the magnetic soft continuum robot (MSCR), characterized by a total length L , magnetic tip length L_m , and cross-sectional radius r_0 . The centerline is modeled as a magneto-elastic rod (denoted as s), with a primary focus on its bending, stretching, and twisting behaviors.

Kinematics. As shown in Fig. 2(A), a MSCR is considered as a slender rod of length L and radius r_0 , characterized by the second moment of area $I = \pi r_0^4/4$, the second polar moment of area $J = \pi r_0^4/2$, and the cross-sectional area $A = \pi r_0^2$. The rod is made of isotropic and linearly elastic material with Young's modulus E , shear modulus G , and density ρ . The length of the magnetic tip is denoted as L_m . Due to its slenderness, i.e., $L \gg r_0$, the rod can be represented by a 1D space curve parameterized by its longitudinal coordinate s (Fig. 2(B)). Its configuration can be described the centerline $\mathbf{r}(s)$ and an accompanying material frame $\{\mathbf{m}_1(s), \mathbf{m}_2(s), \mathbf{m}_3(s)\}$, where

$$\mathbf{m}_3(s) = \frac{\mathbf{r}'(s)}{\|\mathbf{r}'(s)\|}, \quad (1)$$

is the tangential director, and the other two directors are orthonormal to the tangent, i.e.,

$$\begin{aligned} \mathbf{m}_1(s) \cdot \mathbf{m}_2(s) &= 0 \\ \mathbf{m}_1(s) \times \mathbf{m}_2(s) &= \mathbf{m}_3(s). \end{aligned} \quad (2)$$

Hereafter, we use $()'$ to indicate the gradient concerning space s , use $\dot{()}$ to indicate the derivative with respect to time t , and a bar on top $\bar{()}$ represents the evaluation in the undeformed configuration, e.g., $\bar{\mathbf{r}}(s)$ is the

centerline of the reference configuration and $\{\bar{\mathbf{m}}_1(s), \bar{\mathbf{m}}_2(s), \bar{\mathbf{m}}_3(s)\}$ is the material frame of the reference configuration. The rod centerline is assumed to be inextensible, i.e.,

$$\forall s, \varepsilon(s) = 0, \quad (3)$$

where $\varepsilon(s)$ is the uniaxial strain of the centerline,

$$\varepsilon(s) = \|\mathbf{r}'(s)\| - 1. \quad (4)$$

The rotation gradient of the centerline is formulated as

$$\begin{aligned} \mathbf{m}'_1(s) &= \boldsymbol{\omega}(s) \times \mathbf{m}_1(s), \\ \mathbf{m}'_2(s) &= \boldsymbol{\omega}(s) \times \mathbf{m}_2(s), \\ \mathbf{m}'_3(s) &= \boldsymbol{\omega}(s) \times \mathbf{m}_3(s), \end{aligned} \quad (5)$$

where $\boldsymbol{\omega}$ is the so-called Darboux vector,

$$\boldsymbol{\omega}(s) = \kappa_1(s)\mathbf{m}_1(s) + \kappa_2(s)\mathbf{m}_2(s) + \kappa_3(s)\mathbf{m}_3(s). \quad (6)$$

Here, κ_1 and κ_2 represent the bending curvatures, while κ_3 is the twisting curvature. Overall, the macroscopic strains for the 1D rod are the sum of elastic stretching strain in Eq.(4) and elastic curvatures in Eq.(6).

Total potential energy. A linear constitutive law between the curvatures and the elastic energy is used,

$$\mathcal{E}_{\text{ela}} = \int_0^L \left[\frac{1}{2}EI\kappa_1^2(s) + \frac{1}{2}EI\kappa_2^2(s) + \frac{1}{2}GJ\kappa_3^2(s) \right] ds. \quad (7)$$

where EI is the bending stiffness, and GJ is the torsional stiffness. Also, here we assume the initial curvatures of the rod is zero, i.e.,

$$\bar{\kappa}_i(s) = 0, \text{ with } i \in \{1, 2, 3\}. \quad (8)$$

The 1D reduced magnetic energy functional is given by (Sano et al., 2022; Huang et al., 2023a,b)

$$\mathcal{E}_{\text{mag}} = - \int_0^L [\boldsymbol{\mathcal{M}}(s) \cdot \mathbf{B}_a(s)] ds, \quad (9)$$

where \mathbf{B}_a is the actuation magnetic field, and $\boldsymbol{\mathcal{M}}$ is the magnetization density per unit length of the rod in the deformed configuration, which can be formulated as,

$$\boldsymbol{\mathcal{M}}(s) = [\mathbf{m}_1(s) \otimes \bar{\mathbf{m}}_1(s) + \mathbf{m}_2(s) \otimes \bar{\mathbf{m}}_2(s) + \mathbf{m}_3(s) \otimes \bar{\mathbf{m}}_3(s)] \cdot \bar{\boldsymbol{\mathcal{M}}}(s), \quad (10)$$

where $\bar{\boldsymbol{\mathcal{M}}}$ is the magnetization density per unit length in the undeformed configuration.

Confinement within a lumen. With a longitudinal parameter S , the lumen can be characterized by its centerline $\mathbf{R}(S)$ and inner radius $R(S)$, forming a 3D space \mathcal{S} ,

$$\mathcal{S} = \{\mathbf{P} \in \mathcal{R}^3 : \|\mathbf{P} - \mathbf{R}(S)\| \leq R(S), S \in [S_{\min}, S_{\max}]\}. \quad (11)$$

When the MSCR is pushed within the lumen, the rod centerline of MSCR should be constrained by the tube,

$$\forall s, \mathbf{r}(s) \in \mathcal{S}, \quad (12)$$

Equilibrium equations. The equilibrium equations can be derived using functional variation,

$$\delta\mathcal{E}_{\text{ela}} + \delta\mathcal{E}_{\text{mag}} = \delta\mathcal{E}_{\text{ext}}, \quad (13)$$

where \mathcal{E}_{ext} is the work done by the external loadings. The final version of the governing equations is the statement of force and moment balance under geometric constraints (Sano et al., 2022),

$$\begin{aligned} \mathbf{N}'(s) + \mathbf{f}_{\text{mag}}(s) + \mathbf{f}_{\text{ext}}(s) &= \mathbf{0} \\ \mathbf{M}'(s) + \mathbf{m}_3(s) \times \mathbf{N}'(s) + \boldsymbol{\tau}_{\text{mag}}(s) + \boldsymbol{\tau}_{\text{ext}}(s) &= \mathbf{0} \\ \text{s.t. } \forall s, \mathbf{r}(s) &\in \mathcal{S}. \end{aligned} \quad (14)$$

where \mathbf{f}_{ext} (and $\boldsymbol{\tau}_{\text{ext}}$) is the external force density (external moment density), \mathbf{N} (and \mathbf{M}) is the internal elastic force (and internal elastic moment), and \mathbf{f}_{mag} (and $\boldsymbol{\tau}_{\text{mag}}$) is the magnetic force density (magnetic moment density),

$$\begin{aligned} \mathbf{N}(s) &= N_1(s)\mathbf{m}_1(s) + N_2(s)\mathbf{m}_2(s) + N_3(s)\mathbf{m}_3(s) \\ \mathbf{M}(s) &= M_1(s)\mathbf{m}_1(s) + M_2(s)\mathbf{m}_2(s) + M_3(s)\mathbf{m}_3(s) \\ \mathbf{f}_{\text{mag}}(s) &= \boldsymbol{\mathcal{M}}(s) \cdot \nabla \mathbf{B}_a(s) \\ \boldsymbol{\tau}_{\text{mag}}(s) &= \boldsymbol{\mathcal{M}}(s) \times \mathbf{B}_a(s). \end{aligned} \quad (15)$$

Note that the moment is linearly related to the curvature based on the linear constitutive law in Eq. (7), i.e.,

$$\begin{aligned} M_1(s) &= EI\kappa_1(s) \\ M_2(s) &= EI\kappa_2(s) \\ M_3(s) &= GJ\kappa_3(s). \end{aligned} \quad (16)$$

By specifying the various boundary conditions, the configuration of the rod can be solved with the group of differential equations.

3. Forward numerical simulation

Directly solving Eqs. (14), (15), and (16) with constraints is hard and even impossible. In this section, we present the design of our numerical framework, which is built upon the theoretical modeling presented in Section 2, to simulate the dynamics of a MSCR navigating through confined lumens.

Mechanics of MSCR. We use the discrete elastic rod (DER) algorithm to capture the geometrically nonlinear deformations of MSCR (Bergou et al., 2008, 2010). A slender rod-like MSCR can be described by its centerline and the associated material frame (Fig. 3(A)). To capture its geometrically nonlinear configuration, the continuous body is discretized into N nodes,

$$[\mathbf{x}_1, \mathbf{x}_2, \dots, \mathbf{x}_i, \dots, \mathbf{x}_N], \text{ with } i \in [1, N], \quad (17)$$

which leads to $N - 1$ edge vectors,

$$[\mathbf{e}^1, \mathbf{e}^2, \dots, \mathbf{e}^{N-1}], \quad (18)$$

where

$$\mathbf{e}^i = \mathbf{x}_{i+1} - \mathbf{x}_i, \text{ with } i \in [1, \dots, N - 1]. \quad (19)$$

Hereafter, subscripts are adopted for the quantities associated with nodes, e.g., \mathbf{x}_i , and superscripts are for the quantities associated with edges, e.g., \mathbf{e}^i . Each edge, \mathbf{e}^i , has an orthonormal adapted reference frame, $\{\mathbf{d}_1^i, \mathbf{d}_2^i, \mathbf{d}_3^i\}$, together with a material frame, $\{\mathbf{m}_1^i, \mathbf{m}_2^i, \mathbf{m}_3^i\}$, and both of them share the tangential director,

$$\mathbf{d}_3^i \equiv \mathbf{m}_3^i = \frac{\mathbf{e}^i}{\|\mathbf{e}^i\|}. \quad (20)$$

The rotational difference between two frames along the tangential director is denoted by θ^i , as shown in Fig. 3(B). Nodal positions and twist angles constitute a $4N - 1$ degree-of-freedom (DOF) vector,

$$\mathbf{q} = [\mathbf{x}_1, \theta^1, \mathbf{x}_2, \dots, \mathbf{x}_{N-1}, \theta^{N-1}, \mathbf{x}_N], \quad (21)$$

to describe the deformed configuration of a 1D rod-like object. The strains of a deformed rod comprise three parts: stretching, bending, and twisting. The discrete stretching strain of the i -th edge, \mathbf{e}^i , can be evaluated as

$$\varepsilon^i = \frac{\|\mathbf{e}^i\|}{\|\bar{\mathbf{e}}^i\|} - 1. \quad (22)$$

Here, the quantity with a bar on top indicates its undeformed configuration, i.e., $\|\bar{\mathbf{e}}^i\|$ is the undeformed length of i -th edge vector. Similarly, we use

$$\Delta \bar{l}_i = \frac{1}{2}(\|\bar{\mathbf{e}}^i\| + \|\bar{\mathbf{e}}^{i-1}\|) \quad (23)$$

as the Voronoi length associated with the i -th node. Next, referring to Fig. 3(B), the bending curvature distribution can be evaluated by the curvature binormal that measures the misalignment between two consecutive edges at $\{\mathbf{x}_{i-1}, \mathbf{x}_i, \mathbf{x}_{i+1}\}$ (Bergou et al., 2008, 2010),

$$\begin{aligned} \kappa_{1,i} &= \frac{(\mathbf{m}_2^{i-1} + \mathbf{m}_2^i)}{\Delta \bar{l}_i} \cdot \frac{(\mathbf{e}^{i-1} \times \mathbf{e}^i)}{\|\mathbf{e}^{i-1}\| \cdot \|\mathbf{e}^i\| + \|\mathbf{e}^{i-1} \cdot \mathbf{e}^i\|} \\ \kappa_{2,i} &= -\frac{(\mathbf{m}_1^{i-1} + \mathbf{m}_1^i)}{\Delta \bar{l}_i} \cdot \frac{(\mathbf{e}^{i-1} \times \mathbf{e}^i)}{\|\mathbf{e}^{i-1}\| \cdot \|\mathbf{e}^i\| + \|\mathbf{e}^{i-1} \cdot \mathbf{e}^i\|}, \end{aligned} \quad (24)$$

The twisting strain distribution at the i -th node is measured as,

$$\kappa_{3,i} = \frac{(\theta^i - \theta^{i-1} + m_i^{\text{ref}})}{\Delta \bar{l}_i}, \quad (25)$$

where m_i^{ref} is the reference twist associated with the reference frame and can be computed from a parallel transport via time marching (Jawed et al., 2018). The total elastic potentials of a rod system are the sum of the stretching, bending, and twisting, expressed in its discretized form in terms of the DOF vector \mathbf{q} , as

$$E^{\text{ela}} = (E^s + E^b + E^t), \quad (26)$$

where

$$\begin{aligned} E^s &= \sum_{i=1}^{N-1} \frac{1}{2} EA (\varepsilon^i)^2 \|\bar{\mathbf{e}}^i\|, \\ E^b &= \sum_{i=1}^N \frac{1}{2} EI (\kappa_{1,i})^2 \Delta \bar{l}_i + \sum_{i=1}^N \frac{1}{2} EI (\kappa_{2,i})^2 \Delta \bar{l}_i, \\ E^t &= \sum_{i=1}^N \frac{1}{2} GJ (\kappa_{3,i})^2 \Delta \bar{l}_i. \end{aligned} \quad (27)$$

The elastic force can then be computed as the gradient of the elastic energy,

$$\mathbf{F}^e = -\frac{\partial E^{\text{ela}}}{\partial \mathbf{q}}. \quad (28)$$

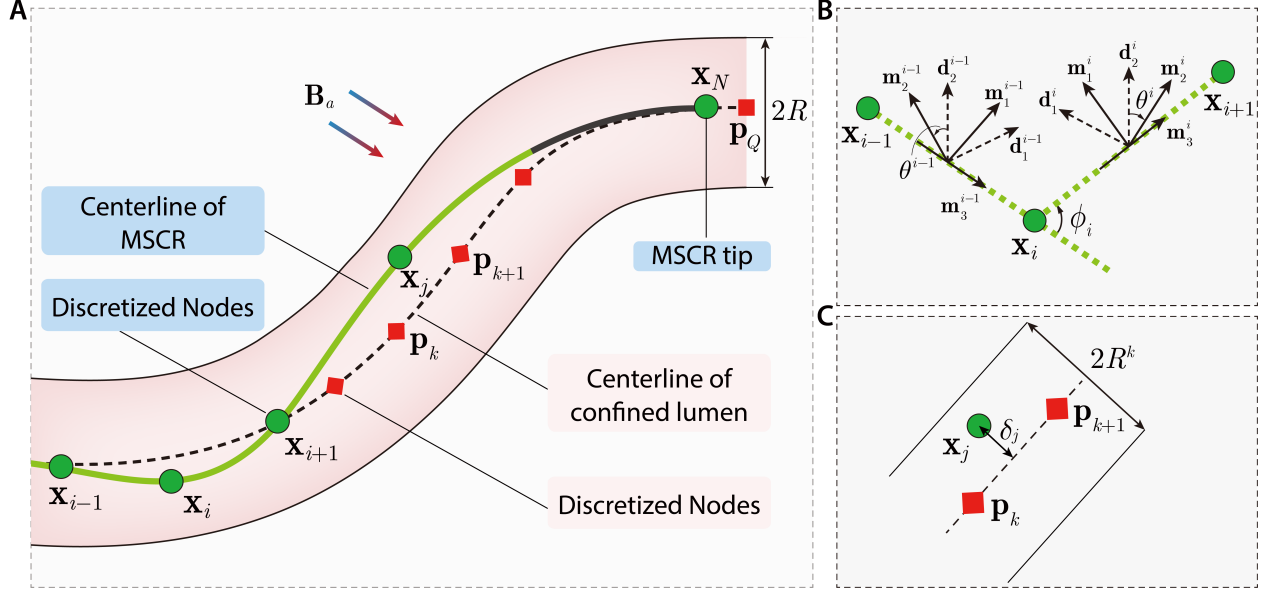


Figure 3: Discretization of the MSCR and confined lumen. The MSCR is discretized as a magneto-elastic rod with the centerline path s , and the confined lumen is approximated as a cylindrical tube with the centerline path S . (A) Discrete diagram of rod (labeled as $\{\mathbf{x}_1, \dots, \mathbf{x}_N\}$) and tube (labeled as $\{\mathbf{p}_1, \dots, \mathbf{p}_M\}$). (B) Discrete measurements for bending and twisting of the rod. (C) Contact model between rod and tube, where δ_j measures the minimal distance from rod node \mathbf{x}_j to the tube path S .

Magnetic actuation. The MSCR with magnetization \mathcal{M} can be actively actuated by the actuation magnetic field \mathbf{B}_a . The discrete format of the magnetic functional is (Huang et al., 2023a,b)

$$E^{\text{mag}} = \sum_{i=1}^{N-1} -(\mathcal{M}^i \cdot \mathbf{B}_a) \|\bar{\mathbf{e}}^i\|, \quad (29)$$

where \mathcal{M}^i is the magnetization vector of i -th edge,

$$\mathcal{M}^i = \left[(\mathbf{m}_1^i \otimes \bar{\mathbf{m}}_1^i + \mathbf{m}_2^i \otimes \bar{\mathbf{m}}_2^i + \mathbf{m}_3^i \otimes \bar{\mathbf{m}}_3^i) \cdot \bar{\mathcal{M}}^i \right]. \quad (30)$$

Finally, the external magnetic force vector can be evaluated in a manner similar to the elastic force vector,

$$\mathbf{F}^{\text{m}} = -\frac{\partial E^{\text{mag}}}{\partial \mathbf{q}}. \quad (31)$$

Contact with a lumen. The MSCR is constrained by a lumen such that the contact constraint needs to be included in the numerical model. The confined lumen is approximated as a curved tube in which the centerline can be described as M nodes,

$$[\mathbf{p}_1, \mathbf{p}_2, \dots, \mathbf{p}_k, \dots, \mathbf{p}_Q], \text{ with } k \in [1, Q], \quad (32)$$

and the local tube radius between the k -th and $(k+1)$ -th node is defined as R^k , which is used for contact deflection and constrained simulation. Note that the tube centerline is assumed to be fixed during the simulation process. The contact element is constructed based on the minimum distance between each node and the tube centerline, and 3 nodes are considered here, i.e., $\{\mathbf{x}_j, \mathbf{p}_k, \mathbf{p}_{k+1}\}$, where \mathbf{p}_k and \mathbf{p}_{k+1} are the vertices on the tube centerline, and \mathbf{x}_j represents j -th node on the MSCR, referring to Fig. 3C. The minimum distance between the j -th node and the tube centerline is defined as δ_j ,

$$\delta_j = \min \left\{ \|\mathbf{x}_j - \mathbf{p}_k\|, \|\mathbf{x}_j - \mathbf{p}_{k+1}\|, \frac{\|(\mathbf{x}_j - \mathbf{p}_k) \times (\mathbf{x}_j - \mathbf{p}_{k+1})\|}{\|\mathbf{p}_k - \mathbf{p}_{k+1}\|} \right\}. \quad (33)$$

To ensure the non-deviation condition between the node and the tube centerline, the following barrier energy function is constructed by (Choi et al., 2021; Tong et al., 2023; Huang et al., 2024)

$$C_j = \begin{cases} -K_c \left[(d_j - \tilde{d})^2 \log(d_j / \tilde{d}) \right] & \text{when } 0 < d_j < \tilde{d} \\ 0 & \text{when } d_j \geq \tilde{d} \end{cases}, \quad (34)$$

where K_c is the stiffness parameter, \tilde{d} is a barrier parameter, and $d_j = R^k - \delta_j$, thus the total contact potential in the sum of contact set \mathcal{C} constructed based on continuous contact detect,

$$E^{\text{con}} = \sum_{j \in \mathcal{C}} C_j. \quad (35)$$

The contact force is the minus gradient of the contact potential, which is expressed as

$$\mathbf{F}^c = -\frac{\partial E^{\text{con}}}{\partial \mathbf{q}}. \quad (36)$$

Equations of motion. Overall, we consider the inertial and damping effects and use a dynamic approach to solve the nonlinear equations. At the k -th time step, t_k , the DOF vector \mathbf{q} can be updated from t_k to $t_{k+1} = t_k + dt$ by imposing the $(4N - 1)$ -sized equation of motion,

$$\begin{aligned} \mathcal{DER} &\equiv \mathbb{M}\ddot{\mathbf{q}}(t_{k+1}) - \mu\mathbb{M}\dot{\mathbf{q}}(t_{k+1}) - dt [\mathbf{F}^e(t_{k+1}) + \mathbf{F}^m(t_{k+1}) + \mathbf{F}^c(t_{k+1})] = 0 \\ \mathbf{q}(t_{k+1}) &= \mathbf{q}(t_k) + dt \dot{\mathbf{q}}(t_{k+1}) \\ \dot{\mathbf{q}}(t_{k+1}) &= \dot{\mathbf{q}}(t_k) + dt \ddot{\mathbf{q}}(t_{k+1}), \end{aligned} \quad (37)$$

where \mathbb{M} is the diagonal mass matrix comprised of lumped masses, μ is the damping coefficient, and dt is the time step size. The iterative Newton-Raphson method is employed to solve the nonlinear equations of motion derived in Eq. (37).

4. Model-based Control Framework

In this section, we define the control problem aimed at ensuring the safe and real-time guidance of a MSCR within confined lumens. The objective is to derive the optimal external magnetic field so that the MSCR's tip can align with the lumen's centerline when the other end of MSCR is pushed with the velocity v_0 into the lumen. In other words, the terminal node of the MSCR should follow the lumen centerline, which results in the following constrained optimization problem:

$$\begin{aligned} \mathbf{B}_a^* &= \arg \min_{\mathbf{B}_a} \|\delta_N\| \\ \text{s.t. } \mathcal{DER}(\mathbf{q}, \mathbf{B}_a) &= \mathbf{0}, \end{aligned} \quad (38)$$

where $\mathbf{B}_a^* \in \mathcal{R}^{3 \times 1}$ is the optimal actuation magnetic field, $\mathcal{DER}(\mathbf{q}, \mathbf{B}_a)$ describes the mechanical response of the MSCR in Eq. (37). In principle, Lagrange multipliers can be introduced for the nonlinear equality constraint to form a Karush–Kuhn–Tucker (KKT) system whose stationarity and feasibility must be satisfied (Ruszczynski, 2011). However, the high dimensionality of the equations of motion $\mathcal{DER}(\mathbf{q}, \mathbf{B}_a)$ and the embedded inequality contact constraints in $\mathcal{DER}(\mathbf{q}, \mathbf{B}_a)$ require active-set updates, which are numerically sensitive and expensive.

To circumvent these difficulties, we propose a model-based control method that leverages the proposed reduced-order simulations and embeds the optimization objective in Eq. (38) into the equilibrium equation itself. Although perfect alignment between the MSCR's tip and the lumen's centerline implies $\delta_N = 0$. Here, we slack this equality constraint to an inequality:

$$\delta_N \leq \xi, \quad (39)$$

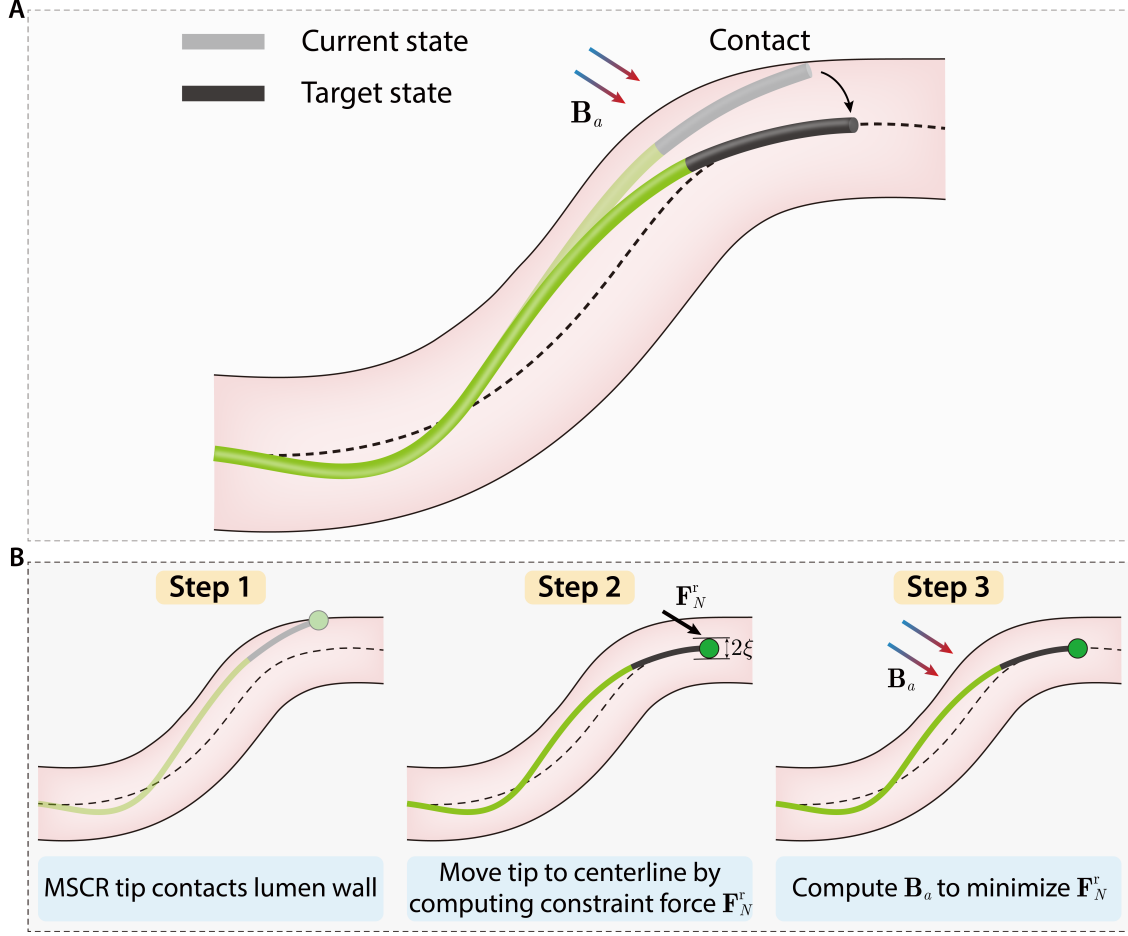


Figure 4: Demonstration of model-based control. (A) Magnetic field control prevents the rod tip from contacting the lumen, highlighting precise manipulation. (B) Control process: Step 1 — detect contact between the rod tip and the lumen; Step 2 — virtually relocate the rod tip to a contact-free region and compute the equivalent constraint force; Step 3 — determine the optimal magnetic field strength to minimize the constraint force and apply it to the current configuration.

As shown in Fig. 4(B), Eq. (39) describes a small “virtual tube” of radius $\xi \ll R$ around the lumen centerline, where R is the local radius of the lumen. To enforce $\delta_N \leq \xi$ without resorting to a direct inequality in the KKT sense, we utilize the contact potential stated in Eq. (34) to compute constraint force applied on the last node $\mathbf{F}_N^r \in \mathcal{R}^{3 \times 1}$. If the tip remains within ξ , the constraint force $\mathbf{F}_N^r \approx \mathbf{0}$. However, as the tip approaches the boundary of the virtual tube, the constraint force, \mathbf{F}_N^r , would “push” it back, effectively encoding the inequality constraint Eq. (39) in the mechanics. Our control objective is to determine the optimal actuation magnetic field \mathbf{B}_a^* that keeps the tip aligned with the tube centerline without exerting any significant constraint force on the small virtual tube. Note that, In other words, this model-based analysis can lead to the following objective function:

$$\mathbf{B}_a^* = \arg \min_{\mathbf{B}_a} \|\mathbf{F}_N^r\| \quad (40)$$

with the following equality constraint:

$$\mathcal{DE}\mathcal{R}(\mathbf{q}, \mathbf{B}_a) + \mathbf{F}^r(\mathbf{B}_a) = \mathbf{0}, \quad (41)$$

where $\mathbf{F}^r \in \mathcal{R}^{(4N-1) \times 1}$ is the constraint force and only non-zero elements are \mathbf{F}_N^r applied on the last node. Note that the constraint force \mathbf{F}_N^r can be computed by solving the updated EOMs stated in Eq. (41).

Therein, we can view Eq. (40) as a root-finding problem on constraint force \mathbf{F}_N^r :

$$\mathbf{F}_N^r(\mathbf{B}_a) = \mathbf{0}. \quad (42)$$

To effectively explore the root of Eq. (42), we employ a finite difference method to compute the numerical Jacobian:

$$\mathbb{J}^{\text{opt}} = \left[\frac{\mathbf{F}_N^r(B_x + \delta e) - \mathbf{F}_N^r(B_x)}{\delta e}, \frac{\mathbf{F}_N^r(B_y + \delta e) - \mathbf{F}_N^r(B_y)}{\delta e}, \frac{\mathbf{F}_N^r(B_z + \delta e) - \mathbf{F}_N^r(B_z)}{\delta e} \right] \quad (43)$$

where $[B_x, B_y, B_z] \equiv \mathbf{B}_a$ is the components of the actuation magnetic field, δe is the small perturbations number. With the computed $\mathbb{J}^{\text{opt}} \in \mathcal{R}^{3 \times 3}$, the Newton search step for updating the actuation magnetic field \mathbf{B}_a can be computed with the momentum-based optimizer:

$$\mathbf{B}_a^{(n+1)} = \mathbf{B}_a^{(n)} - \beta_1 \Delta \mathbf{B}_a^{(n)} - \beta_2 \Delta \mathbf{B}_a^{(n+1)}, \quad (44)$$

where

$$\Delta \mathbf{B}_a^{(n+1)} = (\mathbb{J}^{\text{opt}})^{-1} \mathbf{F}_N^r. \quad (45)$$

Here, β_1 and β_2 are momentum coefficients. When the constraint force \mathbf{F}_N^r is smaller than a threshold, we derive the optimal corresponding external magnetic field \mathbf{B}_a^* and the corresponding updated DOF vector \mathbf{q} , then we move to next time step and continue the pushing process of the MSCR. Thus, the active control process is built within the forward simulation framework. The full algorithm for the model-based control framework is stated in Algorithm 1.

Algorithm 1 Model-based Control Framework

Require: $\mathbf{q}(t_k), \mathbf{B}_a^*(t_k)$ ▷ Current DOFs, actuation magnetic field
Require: ξ, β_1, β_2 ▷ ξ : virtual tube's radius; β_1, β_2 : momentum coefficients
Ensure: $\mathbf{B}_a^*(t_{k+1}), \mathbf{q}(t_{k+1})$ ▷ Optimal magnetic field and updated DOFs of MSCR

- 1: $n \leftarrow 0$
- 2: $\mathbf{B}_a^{(n)} \leftarrow \mathbf{B}_a^*(t_k)$ ▷ Initialize the guess for actuation magnetic field
- 3: $\{\mathbf{F}_N^{r,(n)}, \mathbf{q}^{(n)}\} \leftarrow \mathcal{DE}\mathcal{R}(\mathbf{q}(t_k), \mathbf{B}_a^{(n)}) + \mathbf{F}^{r,(n)}$ ▷ Solve Eq. (41)
- 4: $\Delta \mathbf{B}_a^{(n)} \leftarrow \mathbf{0}$
- 5: **while** $\|\mathbf{F}_N^{r,(n)}\| > \text{tolerance}$ **do**
- 6: $\mathbb{J}^{\text{opt}} \leftarrow \text{Eq. (43)}$
- 7: $\Delta \mathbf{B}_a^{(n+1)} \leftarrow \mathbb{J}^{\text{opt}} \setminus \mathbf{F}_N^{r,(n)}$
- 8: $\mathbf{B}_a^{(n+1)} \leftarrow \mathbf{B}_a^{(n)} - \beta_1 \Delta \mathbf{B}_a^{(n)} - \beta_2 \Delta \mathbf{B}_a^{(n+1)}$
- 9: $n \leftarrow n + 1$
- 10: $\{\mathbf{F}_N^{r,(n)}, \mathbf{q}^{(n)}\} \leftarrow \mathcal{DE}\mathcal{R}(\mathbf{q}(t_k), \mathbf{B}_a^{(n)}) + \mathbf{F}^{r,(n)}$
- 11: **end while**
- 12: $\mathbf{q}(t_{k+1}) \leftarrow \mathbf{q}^{(n)}$
- 13: $\mathbf{B}_a^*(t_{k+1}) \leftarrow \mathbf{B}_a^{(n)}$
- 14: **return** $\mathbf{q}(t_{k+1}), \mathbf{B}_a^*(t_{k+1})$

5. Results

In this section, we present numerical and experimental results to validate our modeling and control framework across different navigation scenarios. We begin by detailing the numerical setup and non-dimensional analysis for parameter normalization. Using the same normalized parameters, we then describe the experimental setup, ensuring consistency between simulations and physical validation. Next, we analyze passive

navigation, where the MSCR is solely pushed by the advancer without an actuation magnetic field. The results reveal increased contact forces and trajectory deviations, demonstrating the limitations of passive control and emphasizing the need for an active control strategy. We then evaluate our model-based control method, showing how it dynamically adjusts the actuation magnetic field to guide the MSCR through confined lumens of varying geometries. The results highlight the framework’s ability to minimize contact forces, maintain stable tip alignment, and ensure precise path tracking, even in complex lumen structures. Finally, we assess the computational efficiency of our approach, demonstrating that the reduced-order numerical model enables real-time updates of the actuation magnetic field, ensuring feasibility for medical and industrial applications. The findings confirm that our method provides an efficient and robust solution for safe and precise MSCR navigation in confined environments.

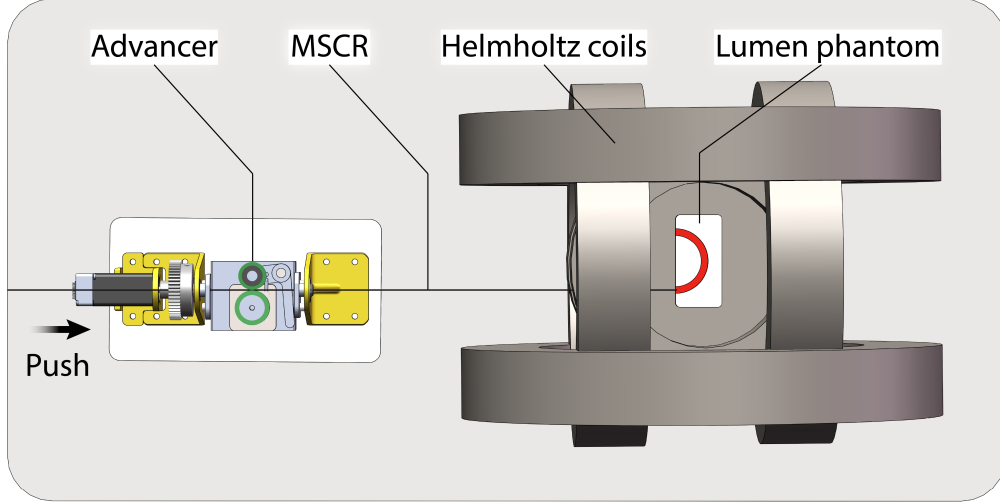


Figure 5: Description of the experiment platform. The lumen phantom is placed in the center of the Helmholtz coils. An advancer clamps the MSCR and then pushes it to navigate the phantom path under the actuating magnetic fields.

5.1. Setup and normalization

Experimental setup. Here we choose a MSCR with a magnetized tip length of $L_m = 5.0$ mm, rod radius $r_0 = 0.6$ mm, and total length $L = 100$ mm. The magnetized tip of MSCR was fabricated by dispersing NdFeB particles (average diameter ~ 5 μ m) in the PDMS matrix (base-to-curing agent mass ratio 10 : 1, Sylgard 184, Dow Corning, USA). The Young’s modulus and shear modulus of the magnetic composite was measured as $E = 3.0$ MPa and $G = 1.0$ MPa, respectively. The MSCR tip was magnetized along its axial direction using impulsed magnetic fields (~ 4 T) generated by a digital pulse magnetizer, resulting in a remanent magnetization $\|\bar{\mathcal{M}}\| = 0.1448$ A·m along the axial direction. As shown in Fig. 5, the experiments were conducted in 3D-printed lumen phantoms placed at the center of Helmholtz coils. The MSCR was pushed by a stepper motor-driven advancer at a controlled speed. The magnitude and direction of actuation magnetic fields were controlled by adjusting the coil currents along three axes. To ensure consistency with the non-dimensional analysis, all applied magnetic fields were normalized for comparative evaluation.

Non-dimensional analysis. To enhance the generalizability of our results and enable broader applicability to various analytical scenarios and provide a side-by-side comparison between the experimental results and numerical predictions, we employ Buckingham’s PI theorem to normalize key variables,

$$\begin{aligned}\mathcal{B} &= \mathbf{B}_a \|\bar{\mathcal{M}}\| L^2 / EI, \\ \mathcal{X} &= v_0 t / L, \\ \mathcal{F} &= \|\mathbf{F}_N^r\| L^2 / EI.\end{aligned}\tag{46}$$

where $\mathcal{B} \equiv [\mathcal{B}_x, \mathcal{B}_y, \mathcal{B}_z]$ is the normalized magnetic field, \mathcal{X} is the normalized push distance, and \mathcal{F} is the normalized tip contact force.

Numerical setup. In our numerical analysis, initially, all discretized nodes and edges are fixed and manually moved at a constant speed, v_0 , along the x -axis, which is defined as the tangential direction at the lumen entrance, until they enter the lumen. Once inside, the constraints are released, allowing the nodes and edges to evolve freely according to the dynamic equilibrium conditions. The physical and geometric parameters of the MSCR in the simulation are selected to match the experimental conditions to ensure a fair evaluation of the model-based control framework in real-world experiments. Also, in numerical study, we adopt the following parameters based on a convergence study: total rod nodal number $N = 100$, total lumen phantom nodal number $Q = 200$, time step size $dt = 10$ ms, contact stiffness $K_c = 1.0$ kPa, contact barrier $\tilde{d} = 0.1$ mm, virtual tube radius $\xi = 0.01R$, and insert speed $v_0 = 1.0$ mm/s. The insertion speed is relatively low compared with the elastic wave to ensure the quasi-static analysis. For model-based control, we use a perturbation magnitude $\delta e = 10^{-4}$ to compute the numerical Jacobian, as well as optimization rate $\beta_1 = 0.9$ and $\beta_2 = 10^{-4}$ for momentum-based gradient optimizer.

5.2. Passive pushing of the MSCR

In this subsection, we examine a case where the MSCR navigates under a passive pushing without magnetic actuation. Two planar cases are considered here: (i) a half-circle lumen phantom, and (ii) a sinusoidal lumen phantom, as both of them are commonly appear in human arteries and veins. We first consider a MSCR moving in a half-circle lumen phantom. The lumen phantom diameter varied in $2R/L \in$

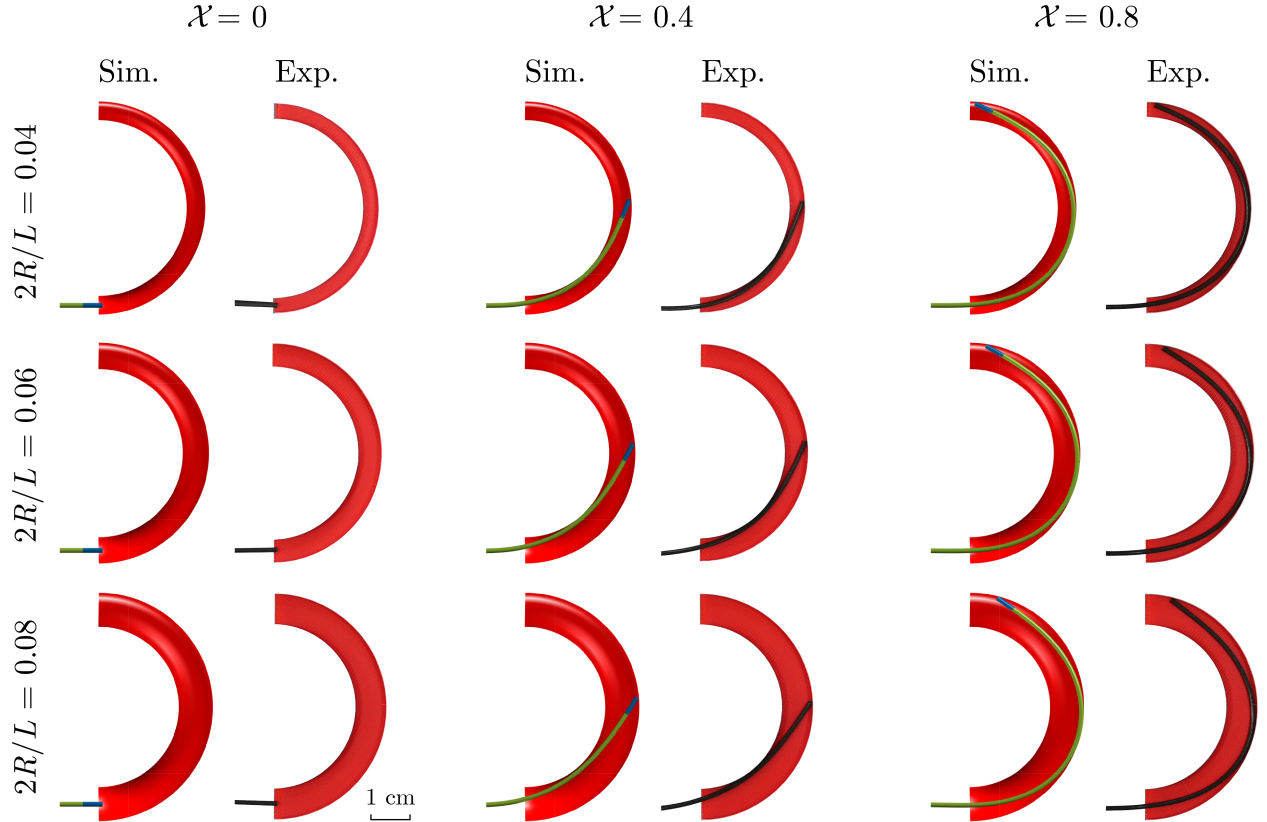


Figure 6: Configurations of MSCR being pushed in half-circle lumen phantoms without magnetic fields in the simulation and experiment, respectively. From top to bottom, the lumen phantom diameters are varied as $2R/L \in \{0.04, 0.06, 0.08\}$.

$\{0.04, 0.06, 0.08\}$, and centerline radius is selected as $\hat{R}_c/L = 0.25$, i.e., the centerline is given by

$$\begin{cases} \hat{X}_c/L &= 0.25 \cos(\omega), \\ \hat{Y}_c/L &= 0.25 \sin(\omega) + 0.25, \end{cases} \quad \text{with } \omega \in [0, \pi]. \quad (47)$$

The comparison between the experiments and the simulation is presented in Fig. 6. The excellent agreement between them validates the physical accuracy of our proposed contact simulation.

Next, a similar scenario for the MSCR moving in a sinusoidal lumen phantom is provided in Fig. 7. Here, the lumen phantom diameter is fixed as $2R/L = 0.06$ and its centerline can be described as,

$$\hat{Y}_s/L = 0.15 \cos(\pi \hat{X}_s/40L) - 0.15, \quad \text{with } \hat{X}_s/L \in [0, 80]. \quad (48)$$

Physical contact between the MSCR and the lumen phantom can be observed and the configuration of the MSCR is determined by both the push distance and the lumen phantom shape. Again, qualitative agreements between the numerical prediction and the experimental observation indicate the accuracy of our discrete model.

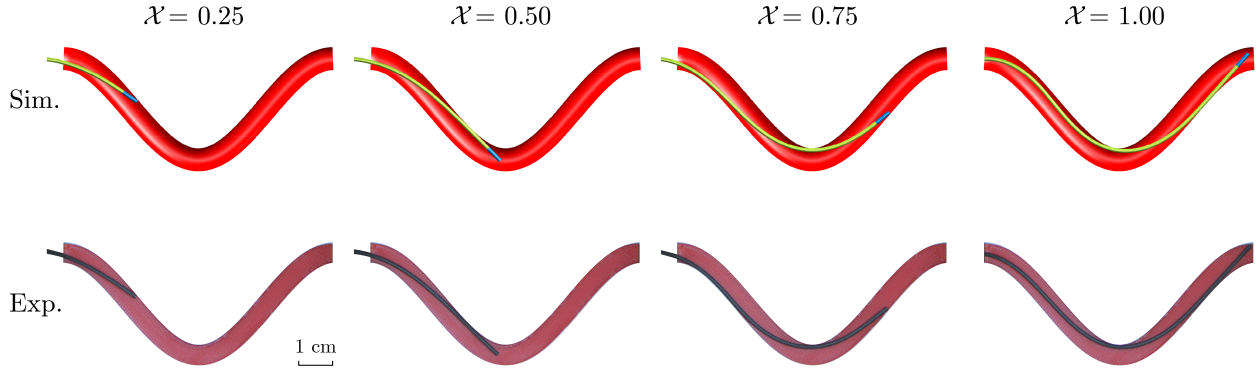


Figure 7: Configurations of MSCR being pushed in a sinusoidal lumen phantom without magnetic fields in the simulation and experiment, respectively. Here, the lumen phantom diameter is $2R/L = 0.06$.

5.3. Active Control of the MSCR Navigating in Planar lumen phantoms

In this subsection, we apply the proposed model-based control algorithm to compute the actuation magnetic field required to navigate the MSCR through the two-dimensional (2D) planar lumen phantoms discussed before: a half-circle and a sinusoidal lumen phantom. We conduct a comprehensive study on how the distal tip contact force varies during navigation to illustrate the effectiveness of the model-based control algorithm. Additionally, desktop experiments are performed to further validate the proposed numerical framework and active control method.

Half-circle lumen phantom. We begin by evaluating the effectiveness of magnetic field control in a commonly encountered half-circle lumen phantom configuration, which mimics the aorta and was previously used for validation in the prior subsection. Here, the lumen phantom geometry is identical to the previous passive pushing analysis, and the lumen phantom diameter is selected as $2R/L = 0.06$. Fig. 8(A) illustrates the navigation of the MSCR with external magnetic control in comparison with the case 2 in Fig. 6, where no magnetic actuation is applied to the system. Our model-based control method effectively regulates the tip's position and orientation, ensuring that the distal contact force \mathcal{F} is eliminated, as shown in Fig. 8(B). The computed optimal actuation magnetic field, shown as a function of the normalized push distance \mathcal{X} in Fig. 8(C), exhibits extreme nonlinearity despite the lumen phantom's constant curvature. This nonlinearity arises from the intricate mechanics of the MSCR, including the coupling between elasticity and magnetic torques, as well as non-smooth contact interactions. These complexities make the optimal control signal

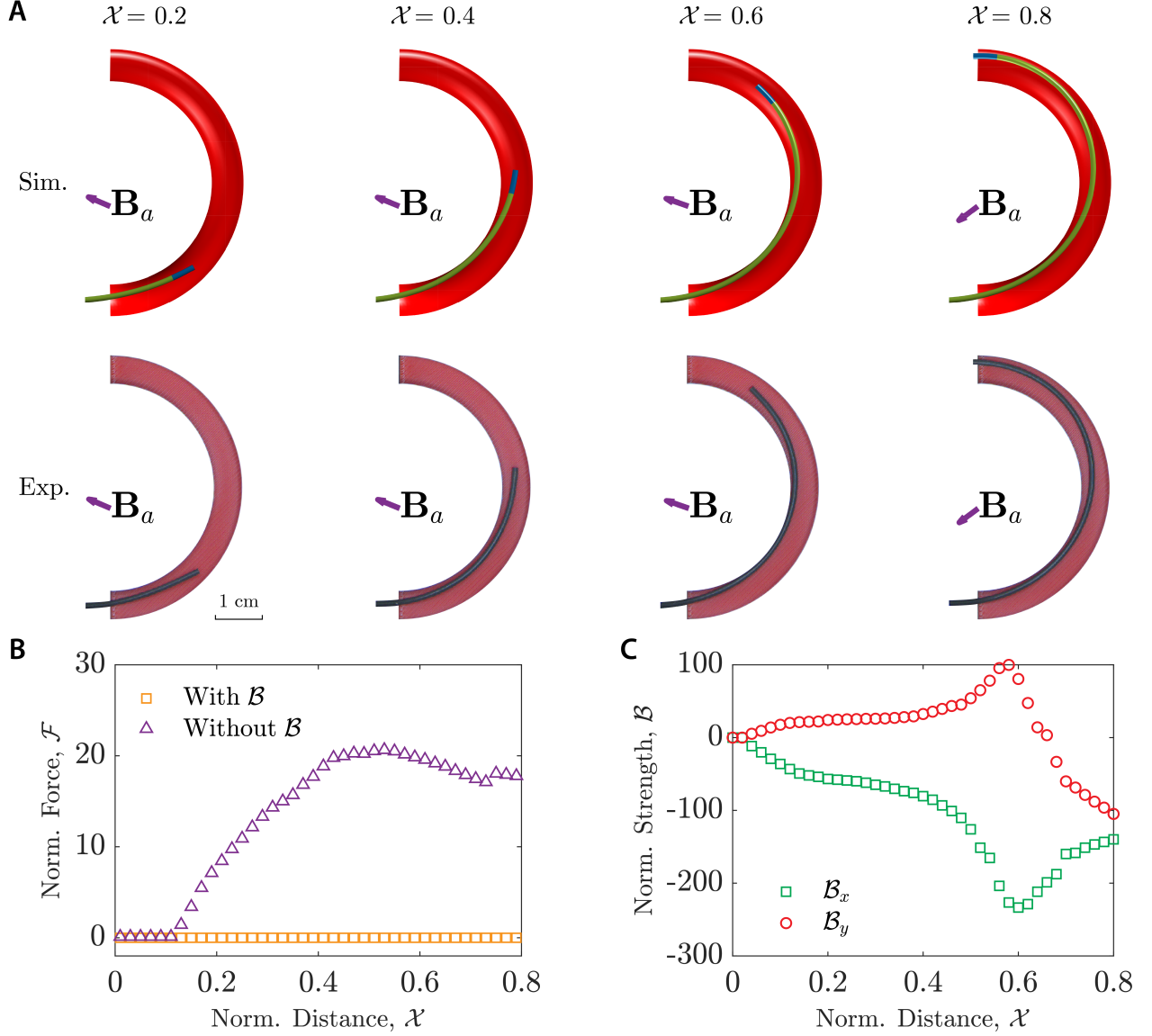


Figure 8: Navigation of MSCR in a half-circle lumen phantom. (A) Tip trajectory of MSCR governed by the controlled magnetic field in the simulation and experiment, respectively. (B) The normalized distal contact force \mathcal{F} plotted against normalized push distance \mathcal{X} . (C) The normalized magnetic field strength \mathcal{B} plotted against normalized push distance \mathcal{X} .

highly nonlinear, further underscoring the challenges of the problem and demonstrating the robustness of the proposed active control scheme. Additionally, the computed optimal magnetic field is validated through desktop experiments (Fig. 8(A)), where no contact between the MSCR’s distal tip and the lumen phantom wall is observed under active control. From a clinical safety perspective, the contact force applied by the MSCR’s tip to lumens should typically remain as small as possible. Our numerical framework suggests that passive pushing of MSCR poses a significant risk to patients due to the excessive tip contact forces. This underscores the necessity of an actuation magnetic field to actively adjust the tip’s position and orientation, ensuring safer navigation.

Sinusoidal lumen phantom. Next, we examine another 2D scenario: a sinusoidal lumen phantom, as discussed before. Again, the lumen phantom geometry is identical to the previous passive pushing analysis. Compared

with the passive pushing shown in Fig. 7, Fig. 9(A) illustrates the tip trajectory of MSCR with the active magnetic field control. As shown in Fig. 9(B), the MSCR contacts the lumen wall initially without magnetic control, resulting in relatively large contact forces. This initial contact stage dissipates when $\mathcal{X} \approx 0.5$, likely because the contact alters the tip's direction slightly (Fig. 7). However, at the valley of the lumen phantom, the tangent angle changes sharply. Without external magnetic actuation to steer the MSCR, the contact forces \mathcal{F} significantly increase to 40. Such high forces could pose a substantial risk of puncturing the lumen wall, especially in vivo. The optimal magnetic field for active control is shown in Fig. 9(C). A pronounced change in the optimal external magnetic field \mathbf{B}_a occurs around $\mathcal{X} \approx 0.5$, which closely aligns with the geometric features of the sinusoidal lumen phantom. Applying this computed magnetic field effectively steers the MSCR through the lumen while maintaining a non-contact state, as validated through both numerical simulations and experimental results.

5.4. Active Control of the MSCR Navigating in 3D lumen phantoms

In this part, we apply the proposed model-based control algorithm to compute the actuation magnetic field required to navigate the MSCR through 3D tubular lumens, providing a more generalized scenario to demonstrate the effectiveness of our approach. Due to experimental limitations, only numerical demonstrations are presented. We investigate the navigation of MSCR in helical lumen phantoms, which commonly appear in coronary arteries, and explore its steerability through bifurcated lumen phantoms to assess control performance in complex vascular environments.

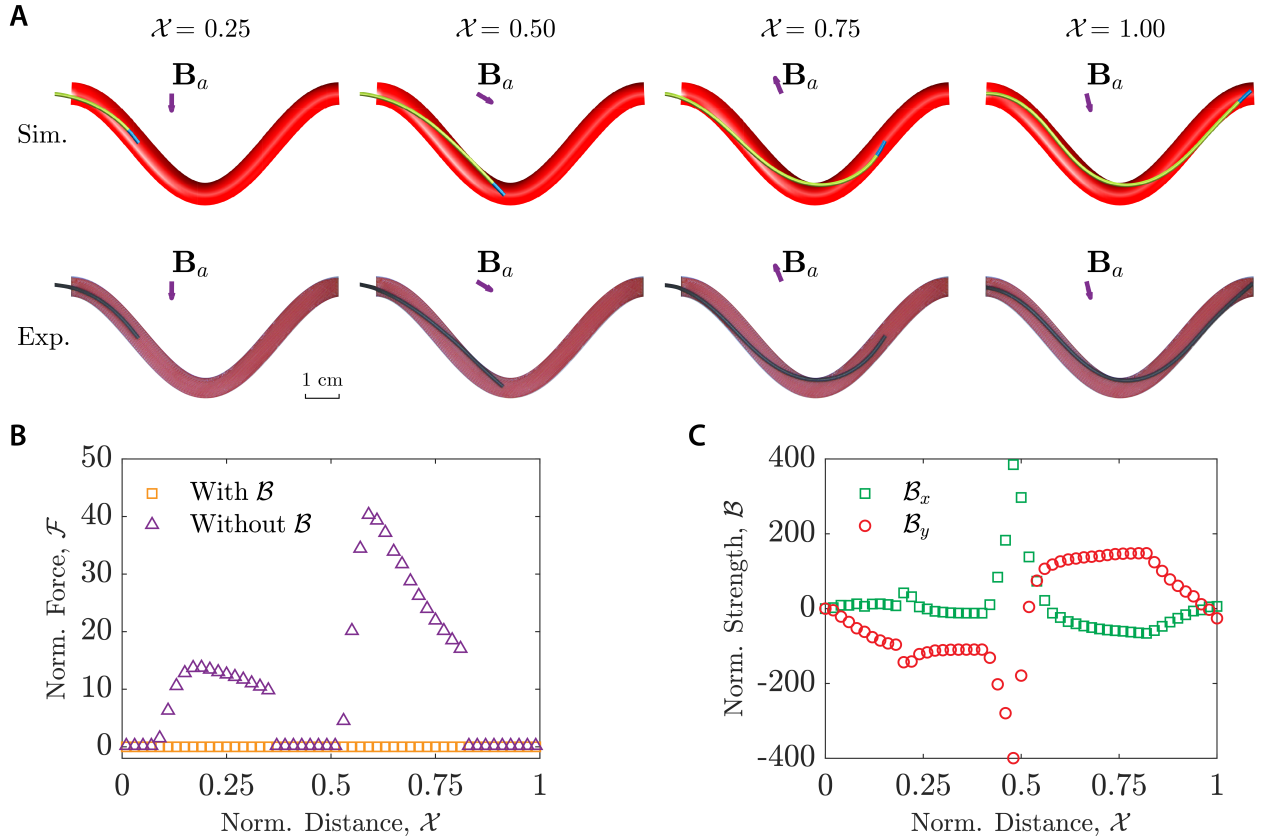


Figure 9: Navigation of MSCR in a sinusoidal lumen phantom. (A) Tip trajectory of MSCR governed by the controlled magnetic field in the simulation and experiment, respectively. (B) The normalized distal contact force \mathcal{F} plotted against normalized push distance \mathcal{X} . (C) The normalized magnetic field strength \mathcal{B} plotted against normalized push distance \mathcal{X} .

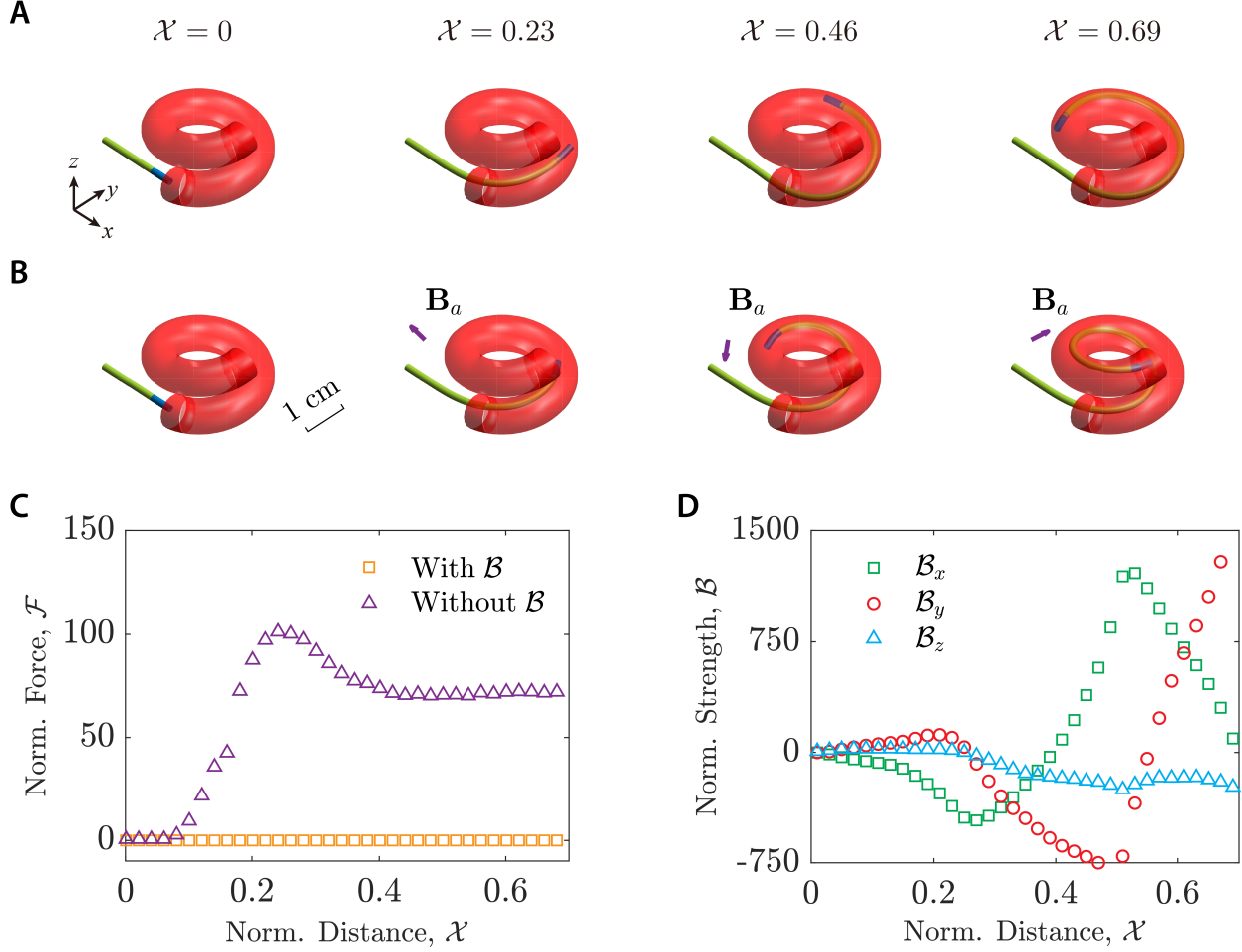


Figure 10: Navigation of MSCR in a helical lumen phantom. (A) Tip trajectory of MSCR governed by the contact interaction in the absence of magnetic field control. (B) Tip trajectory of MSCR governed by the controlled magnetic field. (C) The normalized distal contact force \mathcal{F} plotted against normalized push distance \mathcal{X} . (D) The normalized magnetic field strength \mathcal{B} plotted against normalized push distance \mathcal{X} .

Helical lumen phantom. The helical lumen phantom is characterized by a radius of $\hat{R}_h/L = 0.1$, a pitch of $\hat{\lambda}_h/L = 0.1$ (thus $\hat{P}_h = \hat{\lambda}_h/2\pi$), and total length of $\hat{S}_h/L = 0.9$, resulting in

$$\begin{cases} \hat{X}_h/L &= \hat{R}_h \cos(\omega - \frac{\pi}{2})/L, \\ \hat{Y}_h/L &= \hat{R}_h \sin(\omega - \frac{\pi}{2})/L + \hat{R}_h/L, \\ \hat{Z}_h/L &= \hat{P}_h \omega/L, \end{cases} \quad \text{with } \omega \in [0, \frac{\hat{S}_h}{\sqrt{\hat{R}_h^2 + \hat{P}_h^2}}], \quad (49)$$

and the lumen phantom diameter is $2R/L = 0.06$. Figs. 10(A) and (B) illustrate the tip trajectories with and without magnetic field control, respectively. As shown in Fig. 10(C), the maximum normalized contact force \mathcal{F} is significantly higher than in planar cases, highlighting the increased risk of the MSCR's tip puncturing the lumen wall due to the complex geometry of the lumen phantom. However, with the computed actuation magnetic field shown in Fig. 10(D), our active control method effectively prevents contact between the MSCR's distal tip and the lumen phantom wall, thereby eliminating the contact force \mathcal{F} .

Multi-bifurcated lumen phantoms. The model-based control method not only navigates the MSCR through curved lumen phantoms but also enables it to select the correct branch when encountering multi-bifurcated

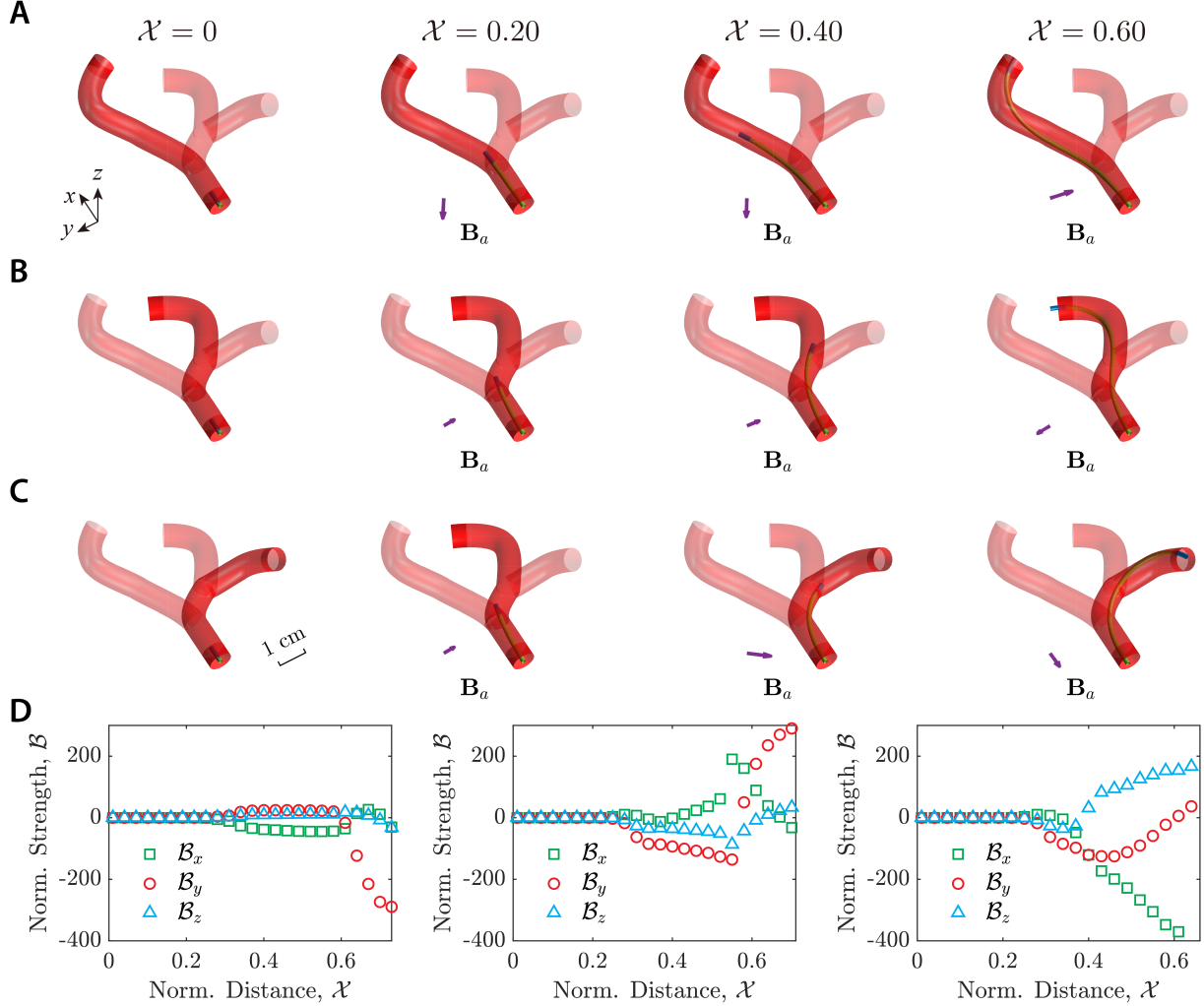


Figure 11: Magnetic navigation of MSCR in the multi-bifurcated lumen phantoms. (A) Left branch. (B) Middle branch. (C) Right branch. (D) The normalized magnetic field strength \mathcal{B} plotted against normalized push distance \mathcal{X} for three branches.

junctions, which are common in the human circulatory system. Here, we present a 3D lumen phantom with three branches, as shown in Fig. 11, and the lumen phantom diameter is $2R/L = 0.06$. Using the proposed model-based control method, we compute the optimal magnetic field to steer the MSCR's tip along one of the three branches, left, middle, or right, based on specific requirements. This demonstrates the versatility of the control strategy in navigating MSCR within complex yet realistic in-vivo environments.

5.5. Computational speed analysis

The accuracy of the proposed numerical framework and the model-based control method have been comprehensively studied in this manuscript. Here, We conduct a full analysis on the computational efficiency of the proposed methodology.

First, we evaluate the proposed reduced-order framework for simulating the passive pushing of the MSCR. As shown in Fig. 12 A, our simulation framework can support large time steps, e.g., $dt \leq 0.1$ s for all cases studied in this manuscript. This benefits from its fully implicit numerical formulation. Notably, when $dt > 0.003$ s, the relative compute time, which is defined as the ratio between the computational time and the simulation clock time, falls below 1.0. This indicates that our simulation not only achieves but

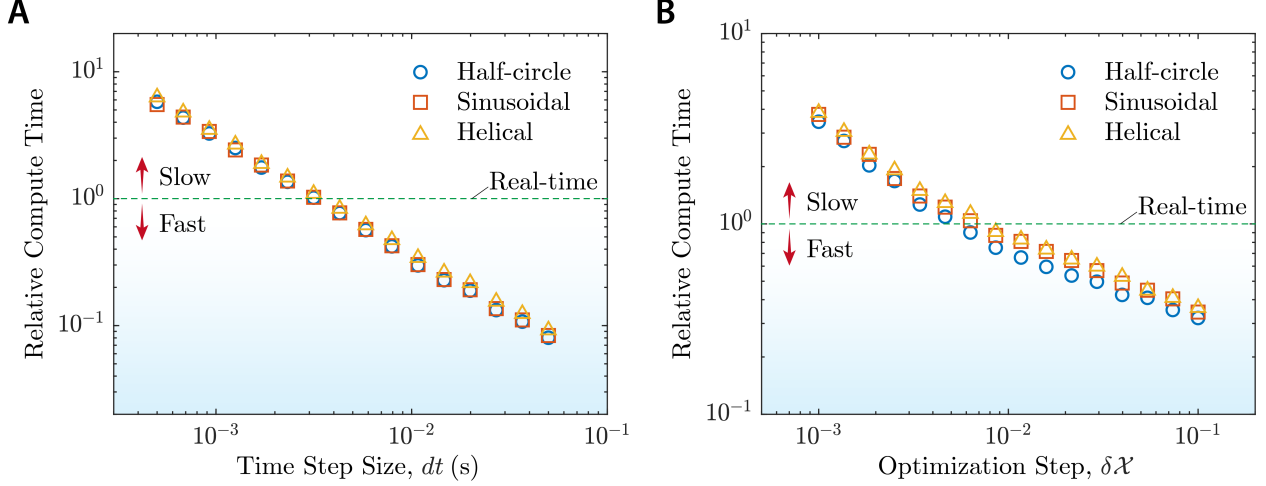


Figure 12: (A) Relative compute time, which is the ratio between the computational time and the simulation clock time, as a function of time step size. (B) Relative compute time as a function of optimization step.

also surpasses real-time performance. The computational efficiency of the numerical framework lays the foundation for the real-time performance of the proposed model-based control methodology. Next, in Fig. 12 B, we study the computational efficiency of the proposed active control method. Here, the optimization step, $\delta\mathcal{X}$, represents the normalized displacement of the tip in the lumen phantom between two consecutive updates of the actuation magnetic field. Here, the normalized total length of MSCR is $\mathcal{X} = 1.0$. In all three cases, we find that our model-based control method can effectively eliminate contact if $\delta\mathcal{X} \leq 0.1$. In addition, when $\delta\mathcal{X}$ is larger than 0.005, the model-based control can achieve real-time performance. These findings demonstrate that our approach strikes an optimal balance between computational efficiency and accuracy, enabling real-time MSCR applications in clinical intervention procedures.

6. Conclusions

In this paper, we present a model-based control framework for navigating MSCR in confined lumens. Building on hard-magnetic elastic rod theory, we developed a reduced-order simulation framework that accurately captures the geometrically nonlinear magneto-elastic deformation and boundary nonlinear contact interactions for MSCR navigating through lumen phantoms. Next, we effectively integrate control constraints into the mechanics model, enabling real-time model-based control while leveraging the computational efficiency of our reduced-order numerical simulations. Our proposed control framework computes the required actuation magnetic field to regulate the MSCR's distal tip, ensuring contact-free navigation within the lumen phantom. This approach significantly mitigates the risks associated with MSCR applications in intervention procedures, enhancing both safety and reliability. The proposed model-based control method was rigorously validated through numerical simulations and experimental studies, demonstrating its effectiveness. Our methodology successfully addresses the challenge of utilizing mechanics models for optimal control of MSCRs.

For future work, we plan to integrate the proposed methodology into robotic systems to enable full automation of MSCR applications in clinical intervention procedures. Additionally, our simplified penalty-based energy formulation for solving optimal control problems with mechanics models highlights a promising direction for incorporating the predictive power of classical mechanics into controller design, paving the way for automated solutions in soft matter manipulation.

Acknowledgments

L. Wang acknowledges the support from the National Natural Science Foundation of China (Grant No. 12388101, 12272369). M. Liu acknowledges the start-up funding from The University of Birmingham, UK. W. Huang acknowledges the start-up funding from Newcastle University, UK.

Appendix A. Video

We provide a video as supplementary material to illustrate our result.

References

- Appireddy, R., Zerna, C., Menon, B. K., Goyal, M., 2016. Endovascular interventions in acute ischemic stroke: recent evidence, current challenges, and future prospects. *Current atherosclerosis reports* 18, 1–11.
- Audoly, B., Pomeau, Y., 2000. Elasticity and geometry. In: *Peyresq Lectures on Nonlinear Phenomena*. World Scientific, pp. 1–35.
- Bergou, M., Audoly, B., Vouga, E., Wardetzky, M., Grinspun, E., 2010. Discrete viscous threads. *ACM Transactions on graphics (TOG)* 29 (4), 1–10.
- Bergou, M., Wardetzky, M., Robinson, S., Audoly, B., Grinspun, E., 2008. Discrete elastic rods. In: *ACM SIGGRAPH 2008 papers*. pp. 1–12.
- Chen, W., Wang, L., 2020. Theoretical modeling and exact solution for extreme bending deformation of hard-magnetic soft beams. *Journal of Applied Mechanics* 87 (4), 041002.
- Chen, W., Wang, L., Yan, Z., Luo, B., 2021. Three-dimensional large-deformation model of hard-magnetic soft beams. *Composite Structures* 266, 113822.
- Chen, W., Yan, Z., Wang, L., 2020a. Complex transformations of hard-magnetic soft beams by designing residual magnetic flux density. *Soft Matter* 16 (27), 6379–6388.
- Chen, W., Yan, Z., Wang, L., 2020b. On mechanics of functionally graded hard-magnetic soft beams. *International Journal of Engineering Science* 157, 103391.
- Choi, A., Tong, D., Jawed, M. K., Joo, J., 2021. Implicit contact model for discrete elastic rods in knot tying. *Journal of Applied Mechanics* 88 (5), 051010.
- Dadgar-Rad, F., Hemmati, A., Hossain, M., 2024. A three-dimensional micropolar beam model with application to the finite deformation analysis of hard-magnetic soft beams. *International Journal of Solids and Structures* 290, 112662.
- Dadgar-Rad, F., Hossain, M., 2022. Finite deformation analysis of hard-magnetic soft materials based on micropolar continuum theory. *International Journal of Solids and Structures* 251, 111747.
- Duan, W., Akinyemi, T., Du, W., Ma, J., Chen, X., Wang, F., Omisore, O., Luo, J., Wang, H., Wang, L., 2023. Technical and clinical progress on robot-assisted endovascular interventions: A review. *Micromachines* 14 (1), 197.
- Garcia-Gonzalez, D., Hossain, M., 2021. Microstructural modelling of hard-magnetic soft materials: Dipole–dipole interactions versus zeeman effect. *Extreme Mechanics Letters* 48, 101382.
- Goyal, M., Yu, A. Y., Menon, B. K., Dippel, D. W., Hacke, W., Davis, S. M., Fisher, M., Yavagal, D. R., Turjman, F., Ross, J., et al., 2016. Endovascular therapy in acute ischemic stroke: challenges and transition from trials to bedside. *Stroke* 47 (2), 548–553.

- Gunduz, S., Albadawi, H., Oklu, R., 2021. Robotic devices for minimally invasive endovascular interventions: a new dawn for interventional radiology. *Advanced Intelligent Systems* 3 (2), 2000181.
- Huang, W., Liu, M., Hsia, K., 2023a. Modeling of magnetic cilia carpet robots using discrete differential geometry formulation. *Extreme Mechanics Letters* 59, 101967.
- Huang, W., Liu, M., Hsia, K. J., 2023b. A discrete model for the geometrically nonlinear mechanics of hard-magnetic slender structures. *Extreme Mechanics Letters* 59, 101977.
- Huang, W., Xu, P., Liu, Z., 2024. Dynamic modeling of a sliding ring on an elastic rod with incremental potential formulation. *Journal of Applied Mechanics*, 1–13.
- Hwang, J., Kim, J.-y., Choi, H., 2020. A review of magnetic actuation systems and magnetically actuated guidewire-and catheter-based microrobots for vascular interventions. *Intelligent Service Robotics* 13, 1–14.
- Jawed, M. K., Novelia, A., O'Reilly, O. M., 2018. A primer on the kinematics of discrete elastic rods. Springer.
- Khoshnam, M., Skanes, A. C., Patel, R. V., 2015. Modeling and estimation of tip contact force for steerable ablation catheters. *IEEE Transactions on Biomedical Engineering* 62 (5), 1404–1415.
- Kim, Y., Genevriere, E., Harker, P., Choe, J., Balicki, M., Regenhardt, R. W., Vranic, J. E., Dmytriw, A. A., Patel, A. B., Zhao, X., 2022. Telerobotic neurovascular interventions with magnetic manipulation. *Science Robotics* 7 (65), eabg9907.
- Kim, Y., Parada, G. A., Liu, S., Zhao, X., 2019. Ferromagnetic soft continuum robots. *Science robotics* 4 (33), eaax7329.
- Kim, Y., Zhao, X., 2022. Magnetic soft materials and robots. *Chemical reviews* 122 (5), 5317–5364.
- Li, J., Chen, H., Wang, L., 2024a. Model-guided navigation of magnetic soft guidewire for safe endovascular surgery. *Journal of the Mechanics and Physics of Solids*, 105731.
- Li, J., Wang, L., 2024. Modeling magnetic soft continuum robot in nonuniform magnetic fields via energy minimization. *International Journal of Mechanical Sciences* 282, 109688.
- Li, P., Feng, J., Zhang, X., Fang, D., Zhang, J., Liang, C., 2024b. Modeling and experimental study of the intervention forces between the guidewire and blood vessels. *Medical Engineering & Physics* 127, 104166.
- Li, X., Yu, W., Liu, J., Zhu, X., Wang, H., Sun, X., Liu, J., Yuan, H., 2023. A mechanics model of hard-magnetic soft rod with deformable cross-section under three-dimensional large deformation. *International Journal of Solids and Structures* 279, 112344.
- Liu, J., Yang, Y., Li, M., Xu, F., 2023. A meshfree model of hard-magnetic soft materials. *International Journal of Mechanical Sciences* 258, 108566.
- Martin, J. W., Scaglioni, B., Norton, J. C., Subramanian, V., Arezzo, A., Obstein, K. L., Valdastrì, P., 2020. Enabling the future of colonoscopy with intelligent and autonomous magnetic manipulation. *Nature machine intelligence* 2 (10), 595–606.
- Moezi, S. A., Sedaghati, R., Rakheja, S., 2024. Development of a novel nonlinear model and control strategy for soft continuum robots featuring hard magnetoactive elastomers. *Smart Materials and Structures* 33 (4), 045025.
- Muller, D. W., Shamir, K. J., Ellis, S. G., Topol, E. J., 1992. Peripheral vascular complications after conventional and complex percutaneous coronary interventional procedures. *The American journal of cardiology* 69 (1), 63–68.

- Munich, S. A., Vakharia, K., Levy, E. I., 2019. Overview of mechanical thrombectomy techniques. *Neurosurgery* 85 (suppl_1), S60–S67.
- Ruszczynski, A., 2011. *Nonlinear optimization*. Princeton university press.
- Sano, T. G., Pezzulla, M., Reis, P. M., 2022. A kirchhoff-like theory for hard magnetic rods under geometrically nonlinear deformation in three dimensions. *Journal of the Mechanics and Physics of Solids* 160, 104739.
- Stewart, E. M., Anand, L., 2023. Magneto-viscoelasticity of hard-magnetic soft-elastomers: Application to modeling the dynamic snap-through behavior of a bistable arch. *Journal of the Mechanics and Physics of Solids* 179, 105366.
- Tong, D., Choi, A., Joo, J., Jawed, M. K., 2023. A fully implicit method for robust frictional contact handling in elastic rods. *Extreme Mechanics Letters* 58, 101924.
- Wang, L., Guo, C. F., Zhao, X., 2022. Magnetic soft continuum robots with contact forces. *Extreme Mechanics Letters* 51, 101604.
- Wang, L., Kim, Y., Guo, C. F., Zhao, X., 2020. Hard-magnetic elastica. *Journal of the Mechanics and Physics of Solids* 142, 104045.
- Wang, L., Zheng, D., Harker, P., Patel, A. B., Guo, C. F., Zhao, X., 2021. Evolutionary design of magnetic soft continuum robots. *Proceedings of the National Academy of Sciences* 118 (21), e2021922118.
- Wang, Y., Chen, R. K., Tai, B. L., Xu, K., Shih, A. J., 2015. Study of insertion force and deformation for suturing with precurved niti guidewire. *Journal of Biomechanical Engineering* 137 (4), 041004.
- Wang, Y., Qin, Y., Luo, K., Tian, Q., Hu, H., 2024. Dynamic modeling and simulation of hard-magnetic soft beams interacting with environment via high-order finite elements of ancf. *International Journal of Engineering Science* 202, 104102.
- Wu, S., Hu, W., Ze, Q., Sitti, M., Zhao, R., 2020. Multifunctional magnetic soft composites: A review. *Multifunctional materials* 3 (4), 042003.
- Yan, D., Abbasi, A., Reis, P. M., 2022. A comprehensive framework for hard-magnetic beams: reduced-order theory, 3d simulations, and experiments. *International Journal of Solids and Structures* 257, 111319.
- Yang, X., Zhou, Y., Zhao, H., Huang, W., Wang, Y., Hsia, K. J., Liu, M., 2023a. Morphing matter: From mechanical principles to robotic applications. *Soft Sci* 3 (4), 38.
- Yang, Z., Yang, H., Cao, Y., Cui, Y., Zhang, L., 2023b. Magnetically actuated continuum medical robots: A review. *Advanced intelligent systems* 5 (6), 2200416.
- Yao, J., Cao, Q., Ju, Y., Sun, Y., Liu, R., Han, X., Li, L., 2023. Adaptive actuation of magnetic soft robots using deep reinforcement learning. *Advanced Intelligent Systems* 5 (2), 2200339.
- Ye, H., Li, Y., Zhang, T., 2021. Magttice: A lattice model for hard-magnetic soft materials. *Soft Matter* 17 (13), 3560–3568.
- Zhao, R., Kim, Y., Chester, S. A., Sharma, P., Zhao, X., 2019. Mechanics of hard-magnetic soft materials. *Journal of the Mechanics and Physics of Solids* 124, 244–263.
- Zhao, Y., Mei, Z., Luo, X., Mao, J., Zhao, Q., Liu, G., Wu, D., 2022. Remote vascular interventional surgery robotics: A literature review. *Quantitative Imaging in Medicine and Surgery* 12 (4), 2552.